AIP | Journal of Applied Physics

The feasibility of Sn, In, or Al doped ZnSb thin film as candidates for phase change material

Yimin Chen, Xiang Shen, Guoxiang Wang, Tiefeng Xu, Rongping Wang, Shixun Dai, and Qiuhua Nie

Citation: Journal of Applied Physics **120**, 015301 (2016); doi: 10.1063/1.4955169
View online: http://dx.doi.org/10.1063/1.4955169
View Table of Contents: http://scitation.aip.org/content/aip/journal/jap/120/1?ver=pdfcov
Published by the AIP Publishing

JOURNAL OF APPLIED PHYSICS **120**, 015301 (2016)

The feasibility of Sn, In, or Al doped ZnSb thin film as candidates for phase change material

Yimin Chen,[1,2,3] Xiang Shen,[1,3,a)] Guoxiang Wang,[1,3] Tiefeng Xu,[1,2,3] Rongping Wang,[4] Shixun Dai,[1,3] and Qiuhua Nie[1,3]

[1]*Laboratory of Infrared Material and Devices, Advanced Technology Research Institute, Ningbo University, Ningbo 315211, China*

[2]*Ningbo Institute of Material Technology and Engineering, Chinese Academy of Science, Ningbo 315201, China*

[3]*Key Laboratory of Photoelectric Materials and Devices of Zhejiang Province, Ningbo 315211, China*

[4]*Centre for Ultrahigh Bandwidth Devices for Optical Systems, Research School of Physics and Engineering Australian National University, Canberra, ACT 0200, Australia*

(Received 4 March 2016; accepted 24 May 2016; published online 1 July 2016)

The potentials of Sn, In, or Al doped ZnSb thin film as candidates for phase change materials have been studied in this paper. It was found that the Zn-Sb bonds were broken by the addition of the dopants and homopolar Zn-Zn bonds and other heteropolar bonds, such as Sn-Sb, In-Sb, and Al-Sb, were subsequently formed. The existence of homopolar Sn-Sn and In-In bonds in $Zn_{50}Sb_{36}Sn_{14}$ and $Zn_{41}Sb_{36}In_{23}$ films, but no any Al-Al bonds in $Zn_{35}Sb_{30}Al_{35}$ film, was confirmed. All these three amorphous films crystallize with the appearance of crystalline rhombohedral Sb phase, and $Zn_{35}Sb_{30}Al_{35}$ film even exhibits a second crystallization process where the crystalline AlSb phase is separated out. The $Zn_{35}Sb_{30}Al_{35}$ film exhibits a reversible phase change behavior with a larger E_a (~4.7 eV), higher T_c (~245 °C), better 10-yr data retention (~182 °C), less incubation time (20 ns at 70 mW), and faster complete crystallization speed (45 ns at 70 mW). Moreover, $Zn_{35}Sb_{30}Al_{35}$ film shows the smaller root-mean-square (1.654 nm) and less change of the thickness between amorphous and crystalline state (7.5%), which are in favor of improving the reliability of phase change memory. *Published by AIP Publishing*. [http://dx.doi.org/10.1063/1.4955169]

I. INTRODUCTION

As semiconductor devices continue to scale downward, there is a requirement to explore new memory technology that scales with the development of the portable consumer electronics with less energy and reduced size without degrading the performance of the devices. One of the leading prototypical memories being investigated is phase change memory (PCM) based on remarkable changes in the properties of amorphous and crystalline phases of chalcogenide alloys.[1]

The most widely studied PCM material is chalcogenide $Ge_2Sb_2Te_5$ (GST) with Sb_2Te_3 and GeTe being one of the most popular stoichiometry.[2] However, GST has a low crystallization temperature, insufficient data retention ability, and a slow phase transition speed. In attempts to solve these problems, metallic elements, such as Al,[3] Ag,[4] Sn,[5,6] Bi,[5,7] Zn,[8] In,[9] W,[10] have been incorporated into GST. In addition, some pseudo chalcogenides, such as Sb-based binary GeSb,[11] GaSb,[12] AlSb,[13] SnSb,[14] and ZnSb,[15] have been investigated for phase change materials due to their good performances. Especially, the ZnSb film shows ultra-long data retention.[15] However, the crystallization behavior of ZnSb will degrade the reliability of the interface between phase change layer and electrode for PCM, due to the metastable phase and non-uniform crystalline grains. Therefore, in this paper, some metallic elements, such as Sn, In, or Al that are usually used as the dopants for improving the performance of phase change materials, are introduced into ZnSb alloy. Then, their physical properties, bonding structures, crystallization behaviors, phase transition speed, and reversible phase change abilities, as well as the film surface roughness and the change of the thickness between amorphous and crystalline state are investigated.

II. EXPERIMENTAL

In, Sn, or Al-doped ZnSb films were prepared by magnetron co-sputtering method using separated ZnSb and metal element alloy targets, e.g., In, Sn, and Al. These films were grown on quartz substrates and SiO_2/Si (100). The base and working pressures were set to 2.0×10^{-4} Pa and 0.35 Pa. The compositions of the films were tuned by different sputtering power applied for each target, and determined by Energy Dispersive Spectroscopy (EDS). The relationship between the sputtering powers and the compositions of these ZnSb-based films was shown in Table I. The ZnSb film with the same thickness was prepared for comparison. The film thickness was *in-situ* controlled by a thickness monitor equipped in the chamber and further *ex-situ* measured by Veeco Dektak 150 surface profiler, being about 80 nm. The bonding structure of the films was examined by X-ray Photoelectron Spectroscopy (XPS). The crystallization behavior was studied by X-ray Diffraction (XRD) patterns and Raman spectra. The sheet resistances of the as-deposited films as a function of elevated temperature (non-isothermal) and time at specific temperatures (isothermal) were *in-situ* measured using the

a)Electronic mail: shenxiang@nbu.edu.cn

TABLE I. Relationship between sputtering powers and compositions of ZnSb-based films.

Power (W)			Power (W)		
ZnSb	Sn	Composition (at. %)	ZnSb	In/Al	Composition (at. %)
50	0	$Zn_{49}Sb_{51}$(ZnSb)	50	4	$Zn_{41}Sb_{36}In_{23}$
50	3	$Zn_{50}Sb_{36}Sn_{14}$	50	5	$Zn_{33}Sb_{38}In_{29}$
50	5	$Zn_{42}Sb_{34}Sn_{24}$	30	5	$Zn_{27}Sb_{30}In_{43}$
50	7	$Zn_{38}Sb_{32}Sn_{30}$	50	3	$Zn_{33}Sb_{42}Al_{25}$
50	10	$Zn_{34}Sb_{28}Sn_{38}$	50	5	$Zn_{35}Sb_{30}Al_{35}$
50	15	$Zn_{26}Sb_{23}Sn_{51}$	30	5	$Zn_{29}Sb_{34}Al_{37}$

two-probe method in a homemade vacuum chamber at a heating rate of 40 K/min. The annealing experiments were performed by rapid thermal annealing (RTA) for 10 min under the protection of Ar gas. The incubation and crystallization time were obtained using a nano-second scale static tester (PST-1, NANOSSTORAGE Co. Ltd., Korea). The surface roughness and the change of the thickness in the film were analyzed by Atomic Force Microscopy (AFM) and X-ray Reflectometry (XRR), respectively.

III. RESULTS AND DISCUSSION

Figs. 1(a)–1(c) exhibit the sheet resistance (R_s) as a function of annealing temperature at a heating rate of 40 K/min for Sn, In, Al-doped ZnSb films, respectively. A continuous decrease of R_s can be observed for all these films during the heating process. Moreover, a sudden drop of R_s occurs when the temperature reaches respective crystallization temperature (T_c) for all the films except for $Zn_{33}Sb_{38}In_{29}$ and $Zn_{27}Sb_{30}In_{43}$ in Fig. 1(b). T_c, which is determined by the temperature corresponding to minimum of the first derivative of R_s-T curve, decreases from 240 °C to 80 °C with increasing Sn concentration in Fig. 1(a) for Sn-doped ZnSb. In Fig. 1(b), $Zn_{41}Sb_{36}In_{23}$ film exhibits a sharp decrease of R_s at ~300 °C, but the addition of more In into the ZnSb film results in the disappearance of the sharp decrease in R_s. This might be the metallic element In excessively doped into ZnSb film. In Fig. 1(c), the T_cs of Al-doped ZnSb films maintain at ~250 °C when Al content changes from 26 at. % to 37 at. %. However, the $Zn_{35}Sb_{30}Al_{35}$ film exhibits a higher amorphous resistance and sharper decrease of R_s. In order to compare the effect of the different doping on R_s of ZnSb-based films, we picked out the best film from Figs. 1(a), 1(b), and 1(c), respectively, and plotted them together with ZnSb film as a function of annealing temperature in Fig. 1(d). Some distinguishable features can be found as follows: (1) T_c of $Zn_{41}Sb_{36}In_{23}$ is nearly at 300 °C which is higher than that of pure ZnSb film (~260 °C), while both T_cs of other ZnSb-based films (245 °C for $Zn_{35}Sb_{30}Al_{35}$ and 240 °C for $Zn_{50}Sb_{36}Sn_{14}$) are lower than that of pure ZnSb film; (2) Compared with pure ZnSb film, In- or Al-doped films have higher R_s, while the Sn-doped film exhibits lower R_s at either crystalline or amorphous state; (3) The slight trace of the second R_s drop can be observed for the pure ZnSb and $Zn_{35}Sb_{30}Al_{35}$ films at higher temperature; (4) When the films transform from an amorphous to a crystalline state, the change of R_s in ZnSb, $Zn_{35}Sb_{30}Al_{35}$, and $Zn_{50}Sb_{36}Sn_{14}$ is sharper than that in $Zn_{41}Sb_{36}In_{23}$ film.

Fig. 2 exhibits the results of activation energy of crystalline (E_a) and 10-yr data retention, which determine the amorphous thermal stability. These parameters can be obtained by the extrapolated fitting curve based on the Arrhenius equation[16]

$$t = \tau \exp(E_a/k_B T), \tag{1}$$

where t is the failure time defined as the time when the film resistance decreases to half of its initial value at the specific temperature (T), and τ is a proportional time constant, k_B is

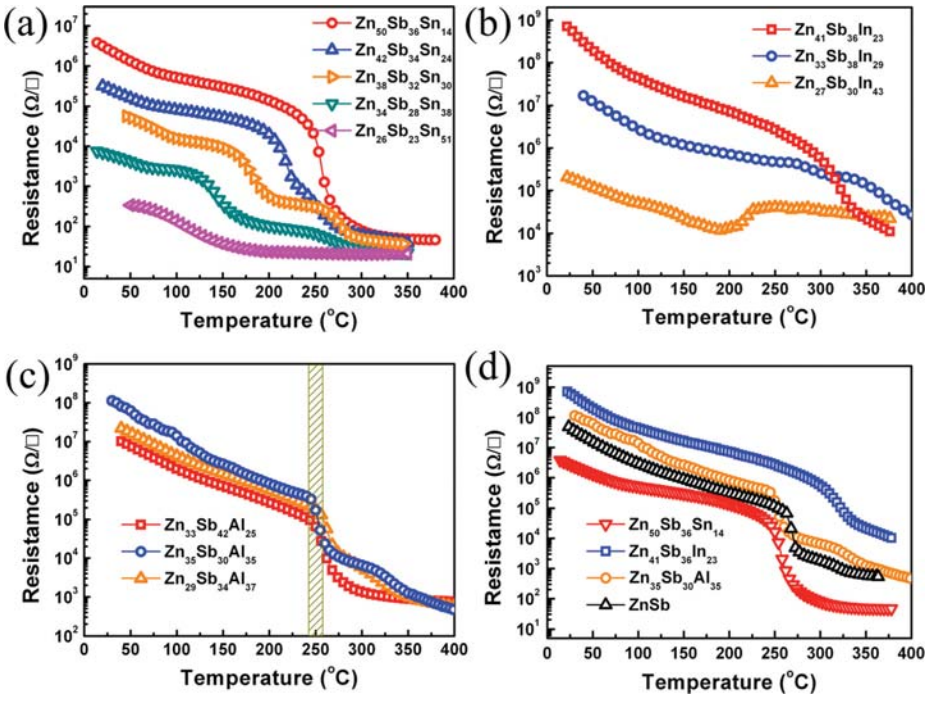

FIG. 1. Sheet resistance as a function of temperature for (a) Sn-doped ZnSb films, (b) In-doped ZnSb films, and (c) Al-doped ZnSb films; (d) sheet resistance as a function of temperature for $Zn_{50}Sb_{36}Sn_{14}$, $Zn_{41}Sb_{36}In_{23}$, $Zn_{35}Sb_{30}Al_{35}$, and pure ZnSb films.

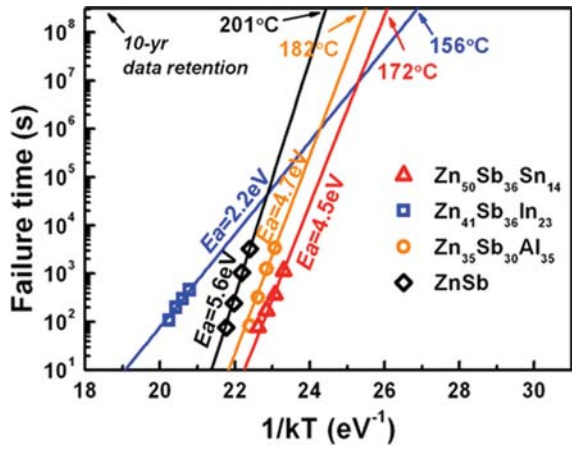

FIG. 2. Arrhenius extrapolation at 10-yr of data retention for $Zn_{10}Sb_{36}Sn_{14}$, $Zn_{41}Sb_{36}In_{23}$ $Zn_{35}Sb_{30}AI_{35}$, and pure ZnSb films.

Boltzmann's constant. The value of E_a is 4.5, 2.2, 4.7, and 5.6 eV for $Zn_{50}Sb_{36}Sn_{14}$, $Zn_{41}Sb_{36}In_{23}$, $Zn_{35}Sb_{30}Al_{35}$, and ZnSb, respectively. The temperatures corresponding to 10-yr data retention, $T_{10\text{-}yr}$, are estimated to be 172, 156, 182, and 201 °C for $Zn_{50}Sb_{36}Sn_{14}$, $Zn_{41}Sb_{36}In_{23}$, $Zn_{35}Sb_{30}Al_{35}$, and ZnSb films, respectively. It appears that $Zn_{35}Sb_{30}Al_{35}$ possesses better thermal stability among these doped-ZnSb films since it has higher T_c, larger E_a, and better 10-yr data retention. In addition, the higher R_s of amorphous state and crystalline state for $Zn_{35}Sb_{30}Al_{35}$ is beneficial to improve the threshold voltage and decrease the RESET current. Furthermore, the first sharper R_s change indicates faster phase transition speed, and the existent of second R_s drop in $Zn_{35}Sb_{30}Al_{35}$ film could realize three-state storage in one PCM cell employing the resistivity difference among the amorphous, metastable, and stable phases.

To confirm whether doped metallic elements are bonded with ZnSb host, we measured the core-level XPS spectra on Zn *2p*, Sb *3d*, and the dopant Sn *3d*, In *3d*, and Al *2p* of as-prepared ZnSb, $Zn_{50}Sb_{36}Sn_{14}$, $Zn_{41}Sb_{36}In_{23}$, and $Zn_{35}Sb_{30}Al_{35}$ films, respectively. All the spectra were normalized to a binding energy of C *1s* at 284.8 eV. Figs. 3(a) and 3(b) are Sb *3d* and Zn *2p* XPS spectra of these films. It is clearly found in Fig. 3(a) that two Sb *3d* peaks for $Zn_{50}Sb_{36}Sn_{14}$ and $Zn_{41}Sb_{36}In_{23}$ films shift towards higher bonding energy, while these peaks for $Zn_{35}Sb_{30}Al_{35}$ film shift slightly towards lower bonding energy compared with the pure ZnSb film. It is well known that the negative shift of the binding energy increases with the decrease of neighboring atom electronegativity, vice versa.[17] The electro-negativities for Sn and In atoms are 1.96 and 1.78, respectively, both of them are larger than that of Zn atom (1.65), while the electro-negativity of Al atom is 1.61 which is slightly smaller than that of Zn atom. Therefore, once the original Zn-Sb bonds are broken by dopant, new heteropolar bonds, such as Sn-Sb, In-Sb, and Al-Sb, will be created, and the different electro-negativities result in the positive or negative shift of the Sb *3d* peak in Fig. 3(a). Fig. 3(b) is the Zn 2*p* spectra for all the films. It was found that Zn *2p* peaks shift towards the lower binding energy after doping, implying that the Zn-Sb bonds are broken by doping and, subsequently, converted into the homopolar Zn-Zn bonds, or other heteropolar bonds such as Zn-Al, Zn-In, and Zn-Sn.

We further decomposed Sn, In, and Al 3d spectra, and the results were shown in Figs. 4(a), 4(b), and 4(c), respectively. Two doublets in Fig. 4(a) clearly indicate that Sn-Sn and Sn-Sb bonds co-exist in the $Zn_{50}Sb_{36}Sn_{14}$ film, and their positions are in good agreement with those in Ref. 14 and support by XPS Handbook.[18] Similarly, In-In and In-Sb bonds co-exist in the $Zn_{41}Sb_{36}In_{23}$ film as shown in Fig. 4(b). Noteworthy is that the content of homopolar Sn-Sn and In-In bonds is more than that of heteropolar Sn-Sb and In-Sb bonds as shown in Figs. 4(a) and 4(b), respectively. However, the binding energy of the Al *2p* XPS spectrum for $Zn_{35}Sb_{30}Al_{35}$ as shown in Fig. 4(c) is 74.9 eV, being higher than that of Al-Al bonds (72.65 eV).[18] The shift of the bonding energy is due to the presence of Al-Sb bonds rather than Al-Al bonds in the $Zn_{35}Sb_{30}Al_{35}$ film. Generally, thermal stability in the amorphous film containing a large amount of homopolar bonds is poor, and a larger E_a is required for the crystallization of the amorphous film containing a large amount of heteropolar bonds. Therefore, we think the value of E_a for $Zn_{35}Sb_{30}Al_{35}$ film is must larger than that of $Zn_{50}Sb_{36}Sn_{14}$ and $Zn_{41}Sb_{36}In_{23}$ films. This is supposed to be well in agreement with the results of amorphous thermal stability, e.g., E_a and 10-yr data retention. It is also interesting to see that the difference in E_a value between $Zn_{41}Sb_{36}In_{23}$ and $Zn_{35}Sb_{30}Al_{35}$ is 2.5 eV, but such a difference becomes almost zero between $Zn_{35}Sb_{30}Al_{35}$ and $Zn_{50}Sb_{36}Sn_{14}$. To understand the physical origin, we also measured the E_a of $Zn_{42}Sb_{34}Sn_{24}$ film, being 2.64 eV (the details are not shown in here). This is close to the E_a value of $Zn_{41}Sb_{36}In_{23}$. Thus, the increase in the E_a value of the $Zn_{50}Sb_{36}Sn_{14}$ film may be ascribed to a small number of Sn content doped into ZnSb

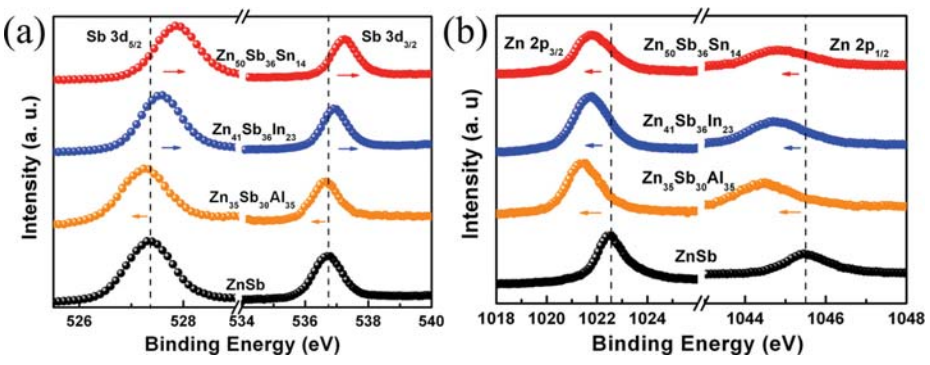

FIG. 3. XPS spectra for $Zn_{50}Sb_{36}Sn_{14}$, $Zn_{41}Sb_{36}In_{23}$, $Zn_{35}Sb_{30}Sn_{35}$, and pure ZnSb amorphous films: (a) Sb *3d* and (b) Zn *2p*.

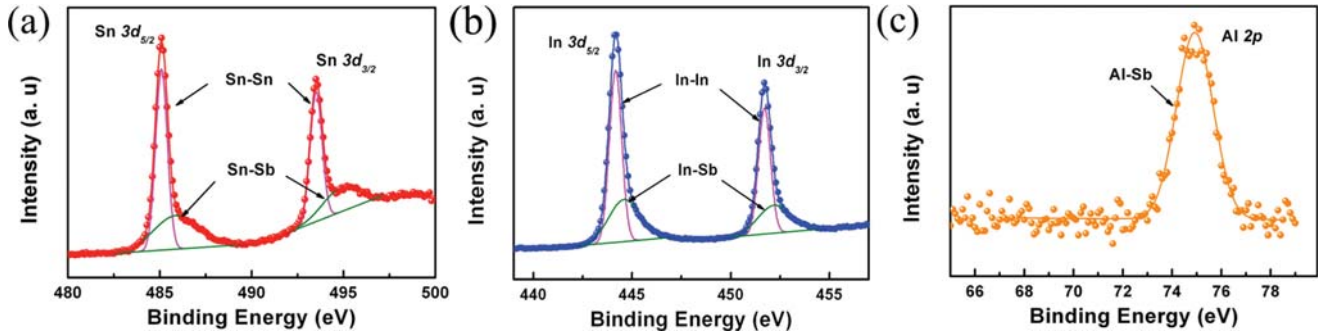

FIG. 4. XPS spectra of (a) Sn *3d*, (b) In *3d*, and (c) A1 *2p* for $Zn_{50}Sb_{36}Sn_{14}$, $Zn_{41}Sb_{36}In_{23}$, and $Zn_{35}Sb_{30}Al_{35}$ amorphous films, respectively.

film, leading to smaller amount of Sn-Sn homopolar bonds in the film.

We also employed XRD to verify the crystallization behavior of the $Zn_{50}Sb_{36}Sn_{14}$, $Zn_{41}Sb_{36}In_{23}$, and $Zn_{35}Sb_{30}Al_{35}$ films. As shown in Fig. 5(a), the amorphous structure in $Zn_{50}Sb_{36}Sn_{14}$ film even annealed at 200 °C is still kept. However, when the film was annealed at 250 °C, the diffraction peaks corresponding to rhombohedral Sb phase (JCPDS No. 1-802) appear. With the further increasing annealing temperature to 300 °C and 350 °C, these Sb diffraction peaks become stronger, implying a further crystallization of the film. Fig. 5(b) shows the XRD curves of the annealed $Zn_{41}Sb_{36}In_{23}$ films. Obviously, the film is still amorphous, even annealed at 300 °C. With further increasing temperature to 350 °C, the film exhibits several broad diffraction peaks corresponding to rhombohedral Sb phases (JCPDS No. 1-802). The XRD curves of the annealed $Zn_{35}Sb_{30}Al_{35}$ films are presented in Fig. 5(c). We can see that the film annealed at 250 °C is still amorphous. However, a crystalline rhombohedral Sb phase (JCPDS No. 1-802) appears in the film annealed at 300 °C, and a cubic AlSb phase (JCPDS No. 79-616) will overlap with those in the film annealed at 350 °C.

Raman spectra of these three films obtained by laser confocal Raman spectrometer are also used to trace the structure evolution of crystallization. The results and their decompositions into different structural units are shown in Fig. 6. There are two broad peaks in the Raman spectrum of the 200 °C-annealed $Zn_{50}Sb_{36}Sn_{14}$ films as shown in Fig. 6(a). The peak at $\sim$114 cm^{-1} can be assigned as E_g mode for Sb-Sb vibration.[19] Another broad peak at 155 cm^{-1} can be decomposed into three peaks at 138, 149, and 170 cm^{-1}, respectively. With increasing annealing temperature to 350 °C, the peak at 114 cm^{-1} becomes stronger due to the fact that the rhombohedral crystalline Sb appears in the film. The Raman spectrum of the $Zn_{41}Sb_{36}In_{23}$ film is presented in Fig. 6(b). A dominant band around 155 cm^{-1} in 250 °C and 300 °C-annealed films can be decomposed into three bands at 133, 153, and 174 cm^{-1}, respectively. When the annealing temperature is increased to 350 °C, a sharp peak appears at 153 cm^{-1}, which can be ascribed to A_{1g} mode in the crystallization of Sb phase.[19] The peak at around 133 cm^{-1} (yellow color in Fig. 6(b)) is due to the In-Sb vibration which is broader than the Sb-Sb vibration peak, especially at 350 °C-annealed film. This is due to the amorphous nature of InSb phase even at 350 °C-annealed film, which is in agreement with the fact that no crystalline InSb phase can be found in the XRD pattern. Let us move to the Raman spectrum of 200 °C and 250 °C-annealed $Zn_{35}Sb_{30}Al_{35}$ film. The whole spectrum can be decomposed into three bands as shown in Fig. 6(c). With increasing annealing temperature to 300 °C, the peak at 155 cm^{-1} becomes sharper, which is due to the appearance of the crystalline Sb phase. When the annealing temperature increases to 350 °C, the peak becomes stronger, indicating that more crystalline Sb grains exist. In addition, a broad peak at 134 cm^{-1} appears in 200 °C-, 250 °C-, and 300 °C-annealed films (yellow color in Fig. 6(c)), which is due to the AlSb amorphous phase in these films. The peak becomes sharper when the annealed temperature is increased to 350 °C. This corresponds to the separation of the crystalline AlSb phase from the film. The evolution of all these Raman spectra is in excellent agreement with the XRD results.

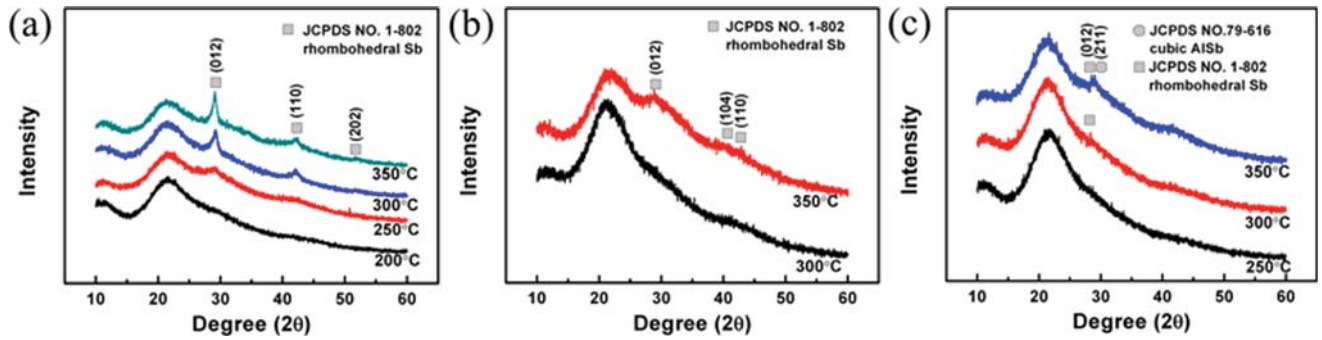

FIG. 5. XRD curves for (a) $Zn_{50}Sb_{36}Sn_{14}$, (b) $Zn_{41}Sb_{36}In_{23}$, and (c) $Zn_{35}Sb_{30}Al_{35}$ films at different annealing temperatures.

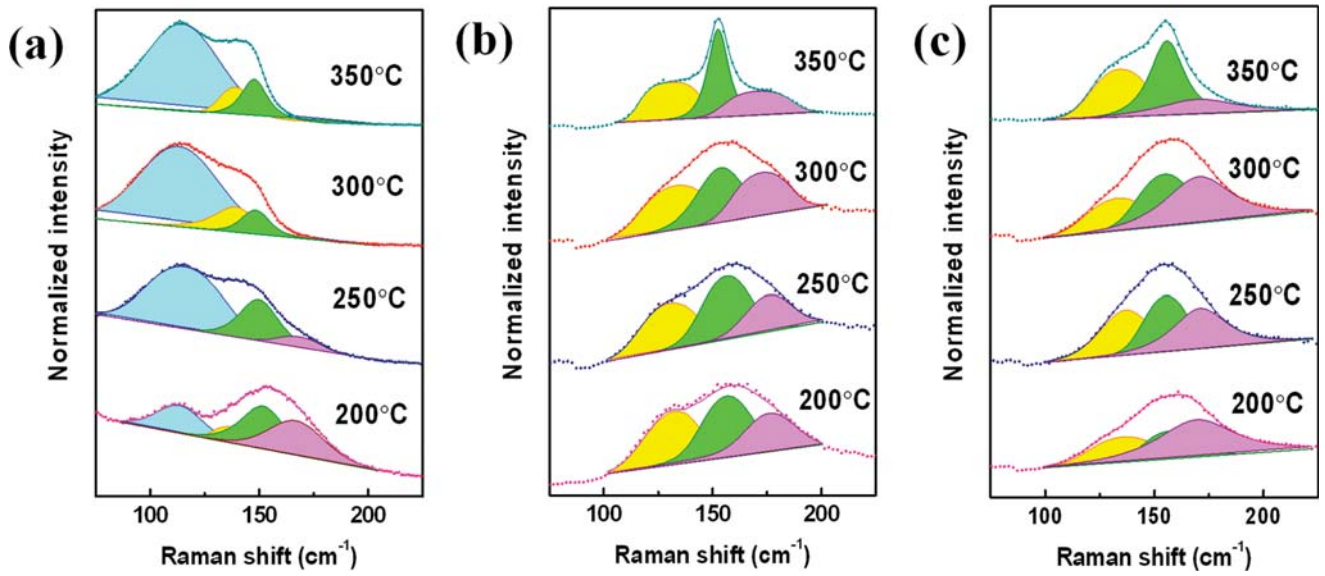

FIG. 6. Raman spectra for (a) $Zn_{50}Sb_{36}Sn_{14}$, (b) $Zn_{41}Sb_{36}In_{23}$, and (c) $Zn_{35}Sb_{30}Al_{35}$ films at different annealing temperatures.

The accurate crystallization time was measured using nano-second scale static tester under laser irradiation. The reflectance (ΔR) of the thin film can be defined by the following equation:

$$\Delta R = (R_{after} - R_{before})/R_{before}, \tag{2}$$

where R_{before} and R_{after} are the reflectivity before and after irradiation, respectively. Figs. 7(a), 7(b), and 7(c) are the Power-Time-Effect (PTE) diagram for $Zn_{50}Sb_{36}Sn_{14}$, $Zn_{41}Sb_{36}In_{23}$, and $Zn_{35}Sb_{30}Al_{35}$ film, respectively. The scale bar in the right of the figures is relative crystallization, defined as the ratio of ΔR to ΔR_{max}. Each PTE diagram can be catalogued into three different regions. (1) The blue region has a relative crystallization below 0.3, where the reflectivity increases smoothly due to insufficient laser power. This process can be called incubation. The incubation time at 70 mW laser power labeled in the diagram is 40, 56, and 20 ns for $Zn_{50}Sb_{36}Sn_{14}$, $Zn_{41}Sb_{36}In_{23}$, and $Zn_{35}Sb_{30}Al_{35}$, respectively. (2) The green region has a relative crystallization between 0.3 and 0.8. The increase of relative crystallization accelerates obviously in this region, due to the continuous formation and growth of the nuclei in the amorphous matrix after incubation. (3) The relative crystallization in the red region is beyond 0.8 and changes slowly due to the growth of the nuclei up to the critical radius. The corresponding time can be considered as complete crystallization time labeled in the diagram (at the laser power of 70 mW), being 142, 134, and 45 ns for $Zn_{50}Sb_{36}Sn_{14}$, $Zn_{41}Sb_{36}In_{23}$, and $Zn_{35}Sb_{30}Al_{35}$, respectively. According to our previous work,[20] the complete crystallization time of GST film, which was obtained by the similar method, is 280 ns. Thus, $Zn_{35}Sb_{30}Al_{35}$ film has faster crystallization speed than that of conventional GST and Sn- or In-doped ZnSb films in this paper.

Let us move to the up-right corner in Fig. 7(c) as marked by the red dash ring. It can be found that the relative crystallization of $Zn_{35}Sb_{30}Al_{35}$ film decreases obviously when the laser pulse power and duration time reach 70 mW and 160 ns, respectively. The enlarged view of this corner is replotted as Fig. 8(a), where the relative crystallization subsequently decreases with increasing pulse duration or laser power. Moreover, the value of ΔR is negative when the pulse power and duration reach 70 mW and 227 ns, indicating that $Zn_{35}Sb_{30}Al_{35}$ film is re-amorphized in their atomic structure.

To examine whether crystallization and re-amorphization are reversible, we performed the optical switching experiments. The ΔR for $Zn_{35}Sb_{30}Al_{35}$ film under repeated laser pulses is shown in Fig. 8(b), where the set power and the pulse width are 40 mW and 250 ns, respectively, for crystallization, and the reset power and pulse width are 70 mW and 250 ns,

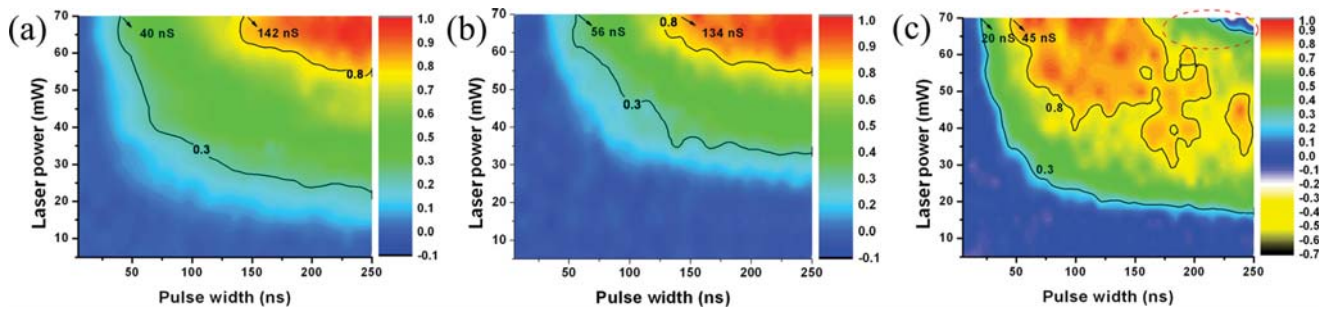

FIG. 7. Power-time-effect plots the nanopulse reflection response in (a) $Zn_{50}Sb_{36}Sn_{14}$, (b) $Zn_{41}Sb_{36}In_{23}$, and (c) $Zn_{35}Sb_{30}Al_{35}$ films.

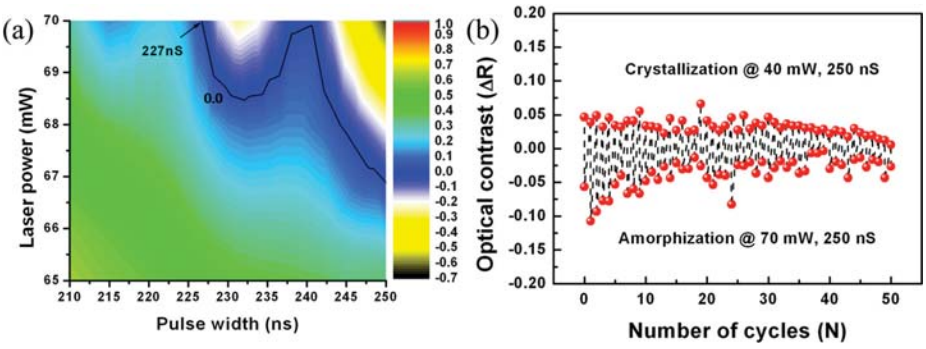

FIG. 8. (a) Enlarged view of marked red dash ring in Fig. 7(c). (b) The optical switching behavior during 50 cycles of operation on the $Zn_{35}Sb_{30}Al_{35}$ film.

respectively, for amorphization. The laser pulses are repeatedly loaded onto the thin film, and this simulates cyclic optical switching upon phase transition. During 50 cycles of the operation, the difference of ΔR between crystallization and amorphization recording is slightly decreased, e.g., the optical reflectivity of amorphous state gradually increases, while that of crystalline state is almost constant. This might be due to the fact that the maximum laser power in our static tester (PST-1) is 70 mW, which is not enough for $Zn_{35}Sb_{30}Al_{35}$ crystalline film to be completely melted in short time. This results in the residual nucleus or crystalline grains that are not completely melted in the re-amorphization process. The number of these residual grains increases with increasing cycle, leading to the gradual increase of the optical reflectivity in amorphous state. Nevertheless, the difference in their ΔR is still obvious to confirm a reversible phase transition process in the $Zn_{35}Sb_{30}Al_{35}$ film.

The surface roughness of the film has a significant impact on device performance because it will affect the quality of the electrode-film interface.[21] Figs. 9(a) and 9(b) show the surface morphology of the AFM images of 300 °C-annealed ZnSb and $Zn_{35}Sb_{30}Al_{35}$ film. The root-mean-square (RMS) surface roughness of the crystalline $Zn_{35}Sb_{30}Al_{35}$ film is 1.654 nm, which is smaller than that of the pure ZnSb film (14.04 nm). The smooth surface in Al-doped film indicates that Al dopant can restrain the grain growth, leading to smaller grain size and lower roughness compared with the pure ZnSb film.

The phase change is always accompanied by an induced stress that could lead to a significant volume change. XRR is an effective way to be used to analyze the thickness, density, and interface of thin film. Fig. 10(a) shows XRR spectra of the as-deposited and 300 °C-annealed $Zn_{35}Sb_{30}Al_{35}$ film. As labeled by the dash lines, the reflection peaks in the crystalline film shift toward the higher angle compared with those in the amorphous film, implying that the thickness of the thin film thickness decreases after crystallization. Here, we used the modified Bragg's equation to evaluate the change of the film thickness[22]

$$\sin^2\theta = 2\sigma + (m + 1/2)^2(\lambda/2h)^2, \tag{3}$$

where σ, m ($m = 1, 2, 3\ldots$), λ, and h are a constant, reflection series, wavelength of Cu K_a radiation (0.154 nm), and film thickness, respectively. Fig. 10(b) shows the plot of $\sin^2\theta$ versus $(m + 1/2)^2$ for the $Zn_{35}Sb_{30}Al_{35}$ film. The correlation of h and the slop k from the fitting lines in Fig. 10(b) is given by the following equation:

$$h = \lambda/2\sqrt{k}. \tag{4}$$

From the XRR data, we can achieve the thickness of the amorphous film is 80 nm, which is in accord with that measured by Veeco Dektak 150 surface profiler. The thickness of the crystalline film is 74 nm. Thus, the change of the film thickness upon crystallization is about 7.5%, which is smaller than that of GST crystallizes into hexagonal phases ($8.2 \pm 0.2\%$).[23] If no material is lost through evaporation, the decrease of the thickness should be positively correlated with the change of the density.[22] Thus, compared with GST,

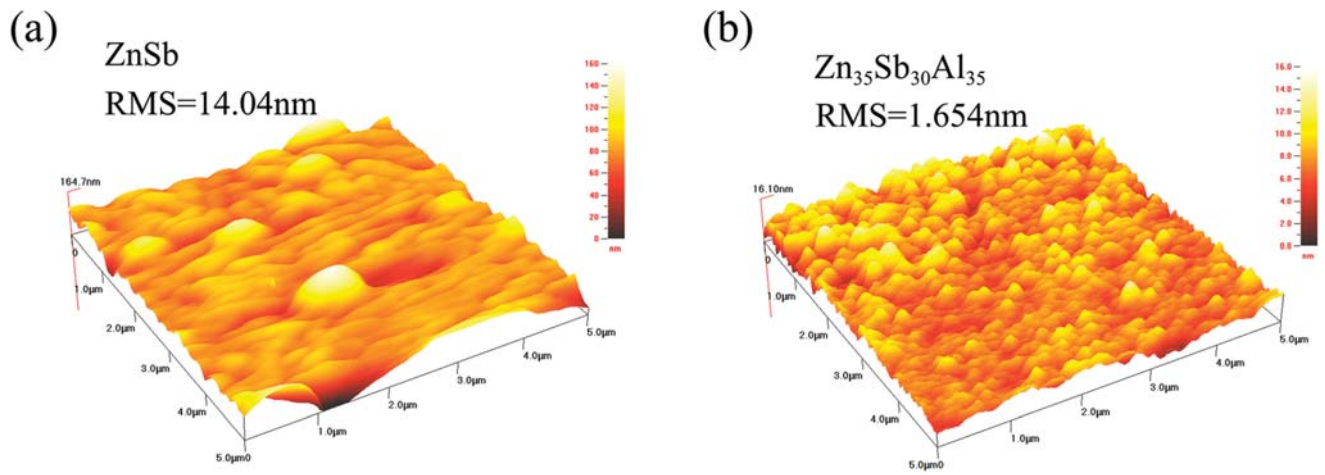

FIG. 9. AFM patterns for 300 °C-annealed (a) ZnSb and (b) $Zn_{35}Sb_{30}Al_{35}$ films.

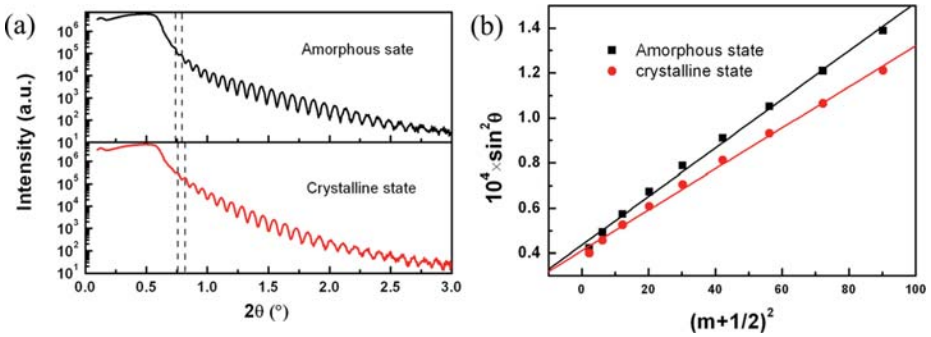

FIG. 10. (a) XRR patterns of $Zn_{35}Sb_{30}Al_{35}$ film; (b) plot of $\sin^2\theta$ versus $(m+1/2)^2$ for $Zn_{35}Sb_{30}Al_{35}$ film.

$Zn_{35}Sb_{30}Al_{35}$ film possesses a smaller density change during the amorphous-to-crystalline phase transition process, which is in favor of the reliability of interface between phase change layer and electrode for PCM.

IV. CONCLUSIONS

In this paper, we investigated the effect of Sn, In, or Al doping on the structure and physical properties of ZnSb film. It was found that the introduction of the metallic dopants such as Sn, In, or Al into ZnSb can break Zn-Sb bonds, and then form new homopolar Zn-Zn bonds and heteropolar Sn-Sb, In-Sb, or Al-Sb bonds. Excess Sn and In were confirmed to present in thin films in the formation of Sn-Sn and In-In bonds in Sn *3d* and In *3d* XPS spectra. In contrast, the Al dopant completely bonds with Sb, forming Al-Sb bonds due to its similar electronegativity between Al and Zn. For thermal stability, the $Zn_{35}Sb_{30}Al_{35}$ film shows higher T_c (~245 °C), larger E_a (~4.7 eV), and better 10-yr data retention (~182 °C). For phase transition speed, the $Zn_{35}Sb_{30}Al_{35}$ film exhibits less incubation time (20 ns at 70 mW), faster complete crystallization speed (45 ns at 70 mW), as well as the reversible characteristic. The surface roughness is 1.654 nm for $Zn_{35}Sb_{30}Al_{35}$, which is smaller than that of pure ZnSb film. The change of thickness between amorphous and crystalline state for $Zn_{35}Sb_{30}Al_{35}$ film is about 7.5%, which is lower than that of GST. The above excellent properties suggest that the $Zn_{35}Sb_{30}Al_{35}$ film could potential be a phase change material for PCM application.

ACKNOWLEDGMENTS

This work was financially supported by the Natural Science Foundation of China (Grant Nos. 61306147, 61377061), the Public Project of Zhejiang Province (Grant No.2014C31146), the Young Leaders of academic climbing project of the Education Department of Zhejiang Province (pd2013092), the Natural Science Foundation of Zhejiang Province (Grant No. LQ15F040002), the Scientific Research Foundation of Graduate School of Ningbo University, and sponsored by K. C. Wong Magna Fund in Ningbo University.

[1]S. R. Ovshinsky, Phys. Rev. Lett. **21**, 1450 (1968).
[2]N. Yamada, E. Ohno, K. Nishiuchi, N. Akahira, and M. Takao, J. Appl. Phys. **69**, 2849 (1991).
[3]G. Wang, X. Shen, Q. Nie, R. Wang, L. Wu, Y. Lv, F. Chen, J. Fu, S. Dai, and J. Li, J. Phys. D: Appl. Phys. **45**, 375302 (2012).
[4]X. Ji-Lin, L. Bo, S. Zhi-Tang, F. Song-Lin, and C. Bomy, Chin. Phys. Lett. **22**, 934 (2005).
[5]T.-J. Park, S.-Y. Choi, and M.-J. Kang, Thin Solid Films **515**, 5049 (2007).
[6]W. Song, L. Shi, X. Miao, and T. Chong, Appl. Phys. Lett. **90**, 091904 (2007).
[7]K. Wang, D. Wamwangi, S. Ziegler, C. Steimer, and M. Wuttig, J. Appl. Phys. **96**, 5557 (2004).
[8]G. Wang, Q. Nie, X. Shen, R. P. Wang, L. Wu, J. Fu, T. Xu, and S. Dai, Appl. Phys. Lett. **101**, 051906 (2012).
[9]K. Wang, C. Steimer, D. Wamwangi, S. Ziegler, and M. Wuttig, Appl. Phys. A **80**, 1611 (2005).
[10]S. Guo, Z. Hu, X. Ji, T. Huang, X. Zhang, L. Wu, Z. Song, and J. Chu, RSC Adv. **4**, 57218 (2014).
[11]C. N. Afonso, J. Solis, F. Catalina, and C. Kalpouzos, Appl. Phys. Lett. **60**, 3123 (1992).
[12]Y. Lu, S. Song, Z. Song, and B. Liu, J. Appl. Phys. **109**, 064503 (2011).
[13]X. Zhou, L. Wu, Z. Song, F. Rao, K. Ren, C. Peng, S. Song, B. Liu, L. Xu, and S. Feng, Appl. Phys. Lett. **103**, 072114 (2013).
[14]F. Rao, Z. Song, K. Ren, X. Li, L. Wu, W. Xi, and B. Liu, Appl. Phys. Lett. **95**, 032105 (2009).
[15]Y. Chen, G. Wang, X. Shen, T. Xu, R. Wang, L. Wu, Y. Lu, J. Li, S. Dai, and Q. Nie, CrystEngComm **16**, 757 (2014).
[16]M. Wuttig and C. Steimer, Appl. Phys. A **87**, 411 (2007).
[17]R. P. Wang, D. Y. Choi, A. V. Rode, S. J. Madden, and B. Luther-Davies, J. Appl. Phys. **101**, 113517 (2007).
[18]C. D. Wagner, W. M. Riggs, L. E. Davis, J. F. Moulder, and G. E. Muilenberg, Handbook of X-ray Photoelectron Spectroscopy (Perkin-Elmer Corporation, Minnesota, 1979).
[19]U. Rossow, U. Frotscher, N. Esser, U. Resch, T. Müller, W. Richter, D. Woolf, and R. Williams, Appl. Surf. Sci. **63**, 35 (1993).
[20]G. Wang, X. Shen, Q. Nie, R. P. Wang, L. Wu, Y. Lu, S. Dai, T. Xu, and Y. Chen, Appl. Phys. Lett. **103**, 031914 (2013).
[21]Y. Hu, S. Li, T. Lai, S. Song, Z. Song, and J. Zhai, J. Alloys Compd. **581**, 515 (2013).
[22]J. Zhang, G. Hernandez, and Y. Zhu, Opt. Lett. **32**, 1317 (2007).
[23]W. K. Njoroge, H. W. Wöltgens, and M. Wuttig, J. Vac. Sci. Technol., A **20**, 230 (2002).